

Structural and particle size evolution of sol–gel-derived nanocrystalline hydroxyapatite

Mohammad Chahkandi¹ · Masoud Mirzaei² 

Received: 26 June 2016 / Accepted: 2 November 2016 / Published online: 12 November 2016
© Iranian Chemical Society 2016

Abstract An easy alkoxide-based sol–gel method based on $\text{Ca}(\text{NO}_3)_2 \cdot 4\text{H}_2\text{O}$ and triethyl phosphate $[\text{PO}(\text{OC}_2\text{H}_5)_3]$; TEP] as Ca and P precursors have been developed to synthesize nano-hydroxyapatite (HA). The structural evolution of the samples was studied using X-ray diffraction (XRD), thermal behavior, infrared analysis, and elemental analysis via scanning electron microscopy. It is noticeable that raising of the firing temperature resulted in increasing the HA content as the dominant phase at 600 and 700 °C. The phase transformation from amorphous to crystalline HA occurred at the low temperature of 400 °C, while at higher temperatures other Ca–P compounds as secondary phases transformed to HA. The crystallite size distributions and micro-strain of the HA samples produced were characterized by XRD methods with the aid of Scherrer and Williamson–Hall equations. The results of transmission electron microscopy as a complementary and reliable technique are in good agreement with those obtained from XRD. The results indicate that increasing the firing temperature caused permanent growth of mean crystallite size and a decrease in micro-strain.

Keywords Nanocrystalline hydroxyapatite · Sol–gel · Scherrer · Williamson–Hall · TEM

Introduction

Hydroxyapatite (HA) is one of calcium phosphate (Ca–P) bio-ceramics which makes up the majority of mineral constituents of human bone and teeth. Because of biocompatibility, bioactivity, osteoconductivity, and compatible structure, and composition to natural hard tissues, synthetic HA has long been recognized as one of the most important bone substitute materials that can be used in implant fabrication [1–5]. Most synthetic apatites are formed via high temperature processes (e.g., sintering), resulting in a well-crystallized structure with big particle size [6–8], having little or no bioresorption activity. This is in contrast to nanocrystalline apatites that exhibit a much higher degree of bio-activity. The basic driving force for crystallization process especially during sintering is a decrease in surface-free energy through the reduction in surface area of the powder [9]. Therefore, smaller amorphous particles with higher surface energy turn to crystalline ones at lower sintering temperatures. The most significant effect of firing temperature is phase transformation leading to changes in lattice parameters; i.e., as our previous work the sintering temperature of sol–gel-derived anhydrous dicalcium phosphate (DCPA) is 300 °C that transforms to HA and β -tricalcium phosphate (β -TCP) at 600 and 1000 °C, respectively [10]. However, other physical and chemical properties like average size, electrochemical performance [11], microstructure, dielectric constant [12], and porosity [13] could be changed. In order to obtain HA with diverse applications [14–18], researchers have tried to customize its properties such as bioactivity, solubility, and sinterability by controlling its structural composition, morphology, and particle size [17–20]. The sol–gel process, because of its well-known inherent advantages such as homogeneous molecular mixing, low processing temperature, and high product purity, became an important

✉ Mohammad Chahkandi
m.chahkandi@hsu.ac.ir

✉ Masoud Mirzaei
mirzaeesh@um.ac.ir

¹ Department of Chemistry, Hakim Sabzevari University, Sabzevar 96179-76487, Islamic Republic of Iran

² Department of Chemistry, Ferdowsi University of Mashhad, Mashhad 917751436, Islamic Republic of Iran

route for generation of HA and other Ca–Ps [10, 21–27]. The low temperature of sol–gel method results in a low crystalline HA containing a mixture of nano-to-submicron crystals better accepted by the host tissue [3]. However, secondary phases such as calcium oxide (CaO) and Ca–Ps are also formed. High temperature formation techniques like post-deposition and thermal-annealing treatments transform Ca–P phases to HA, along with the development of crystallinity and particle size [10, 21, 28–31]. TEM can be applied for direct observation of the particle size determination in the nanometer range, or XRD can be used for measurements of the coherence length of the particles, where the particle size is related to the diffraction peak broadening. The advantage of TEM is clearly the visualization of objects that allows counting of the particle size distribution. However, these statistical data can be unreliable due to the difficulty in counting of small particles [32]. Beside of all available methods, Scherrer's method is a well known one that uses the width of the diffraction peak derived from X-ray patterns. The diffraction peak width depends on the size of crystalline particle, inhomogeneous strain, and instrumental effects. Therefore, determining the crystallite size from powder diffraction data accurately is complicated and hence various indirect methods such as the Williamson–Hall (W–H method) are often used [33] and this inexpensive method provides a very simple possibility for estimating the particle size [23, 34].

Herein, nanoparticles of HA have been synthesized through a novel low temperature alcohol-based sol–gel method using $\text{Ca}(\text{NO}_3)_2 \cdot 4\text{H}_2\text{O}$ and triethylphosphate (TEP) as Ca and P precursors. With the aid of this novel technique some advantages could be highlighted such as: (a) high purity of product due to hydrolysis of TEP before addition to the Ca sol, (b) formation of nanocrystalline HA without using any grinding process. The particle size of nanocrystalline sol–gel-derived HA has been determined by TEM and the modified Scherrer equation (see “[Nanostructural examination](#)” section). Moreover, the effect of firing temperature on the sample purity, particle size, and micro-strain has been investigated. Experimental results showed that the firing temperature could have an effect on the structural evolution of the product while the HA phase can be crystallized at a relatively low temperature (400 °C). The obtained values of crystallite size of HA from W–H and TEM analyses have good consistency.

Materials and methods

Sol–gel synthesis and physical measurement

First, as the novel part of the applied method, TEP was hydrolyzed for 24 h at room temperature (the molar ratio

of water to phosphate is fixed at 8) in a parafilm-sealed glass container under vigorous stirring. Next, 4 M hydrolyzed triethyl phosphate [$(\text{C}_2\text{H}_5\text{O})_3\text{PO}$, TEP, Fluka] was prepared by dilution in anhydrous ethanol. Then, 3 M $\text{Ca}(\text{NO}_3)_2 \cdot 4\text{H}_2\text{O}$ (Merck) dissolved in distilled water was added slowly to the phosphorus sol at a rate of 6 ml/min ($\text{Ca}/\text{P} = 1.67$). The resulting sol solution was continuously agitated for 60 min at 80 °C. The clear solution that was obtained was aged at room temperature for 24 h before drying. In order to better follow the progress of the sol–gel process, the pH values of the sample solutions before and during aging were recorded. These aged sols were then subjected to thermal treatment at 150 °C until a white-dried gel was obtained. The as-prepared gel structure was analyzed using differential thermal analysis (DTA, Netzsch, Germany) and infrared (IR) spectroscopy (Buck 500, KBr) in the range of 500–4000 cm^{-1} . The dried gels were ground with a mortar and pestle into a fine powder and subjected to different calcination temperatures (300, 400, 500, 600, and 700 °C) for 2 h at a constant heat rate of 2 °C/min. Phase identification of the calcined gels (**S1–S5** in Fig. 1a, b) was performed using an X-ray diffractometer (XRD, Philips, X'pert Pro, $\text{Cu K}\alpha$) at a scanning speed of 1° in $2\theta/\text{min}$ from 20° to 45°. The Ca and P contents were measured by scanning electron microscopy (SEM, S 360, Oxford-England) (see Scheme 1; Table 1).

Particle size determination

Particle size and micro-strain of the synthesized HA powders with the aid of Scherrer and W–H equations [33, 35] were calculated. To determine the instrumental line broadening, XRD pattern of a microcrystalline quartz powder as the standard sample was recorded. Also, particle size distribution was determined by TEM observations. TEM (Leo 912 AB-Germany) was equipped with a thermionic gun and was operated at 120 kV. TEM samples were prepared as follows: the HA powder was ultrasonically dispersed for 2 h in absolute ethanol and afterward deposited on a carbonated copper grid.

Results and discussion

Structural evolution

Sol–gel HA samples have been synthesized using precursors of phosphorus alkoxide such as triethyl phosphite and triethyl phosphate, frequently [21, 36–38]. However, herein, as an advantage over other methods [17, 18, 22, 36, 39–41] the hydrolysis of TEP (Eq. 1) resulted in a more complete polymerization reaction of Ca and P (Eq. 2). A continuous pH measurement of the Ca and P mixed

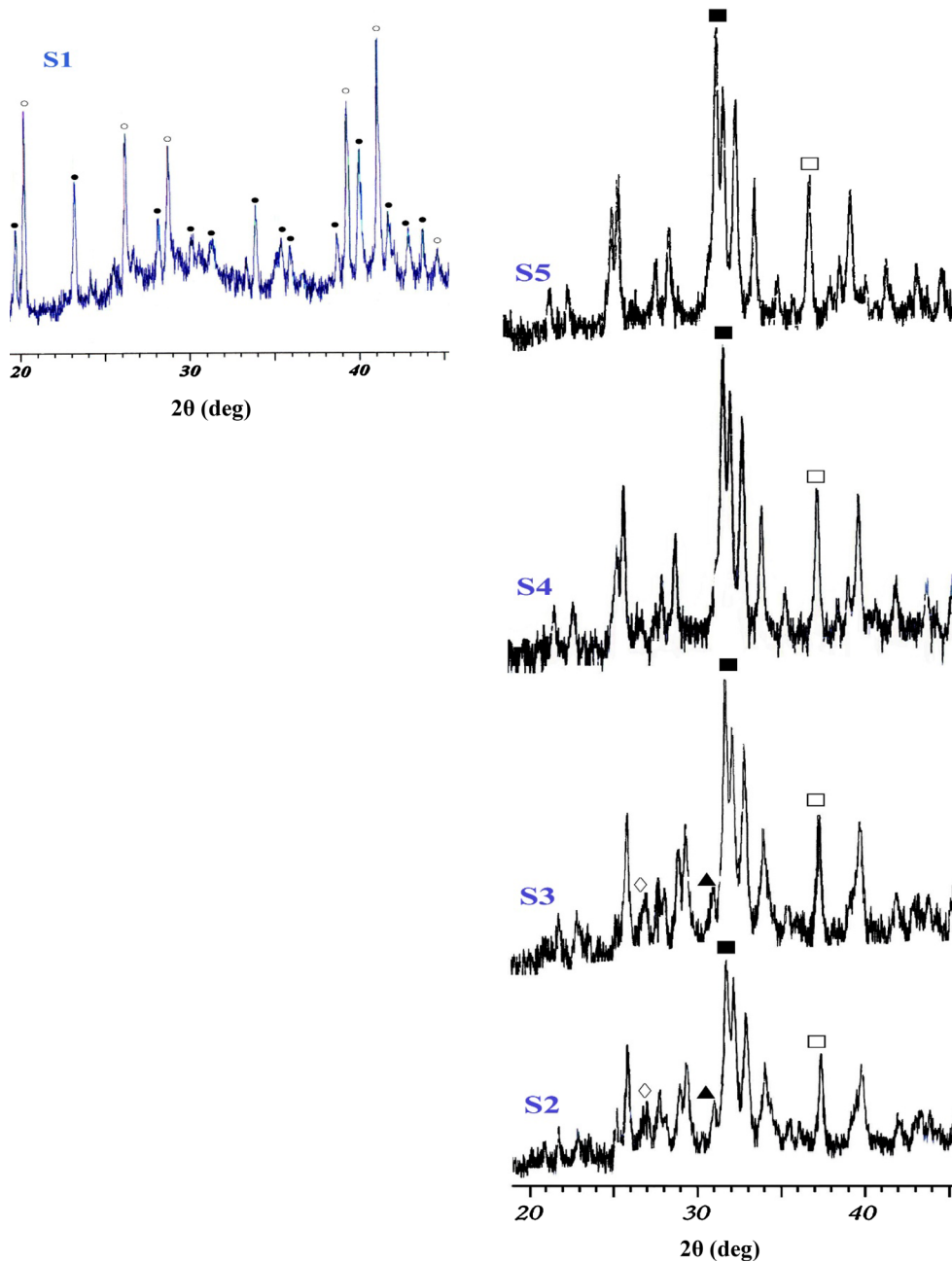
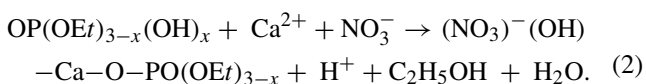
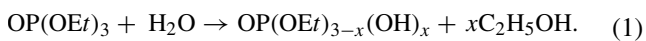
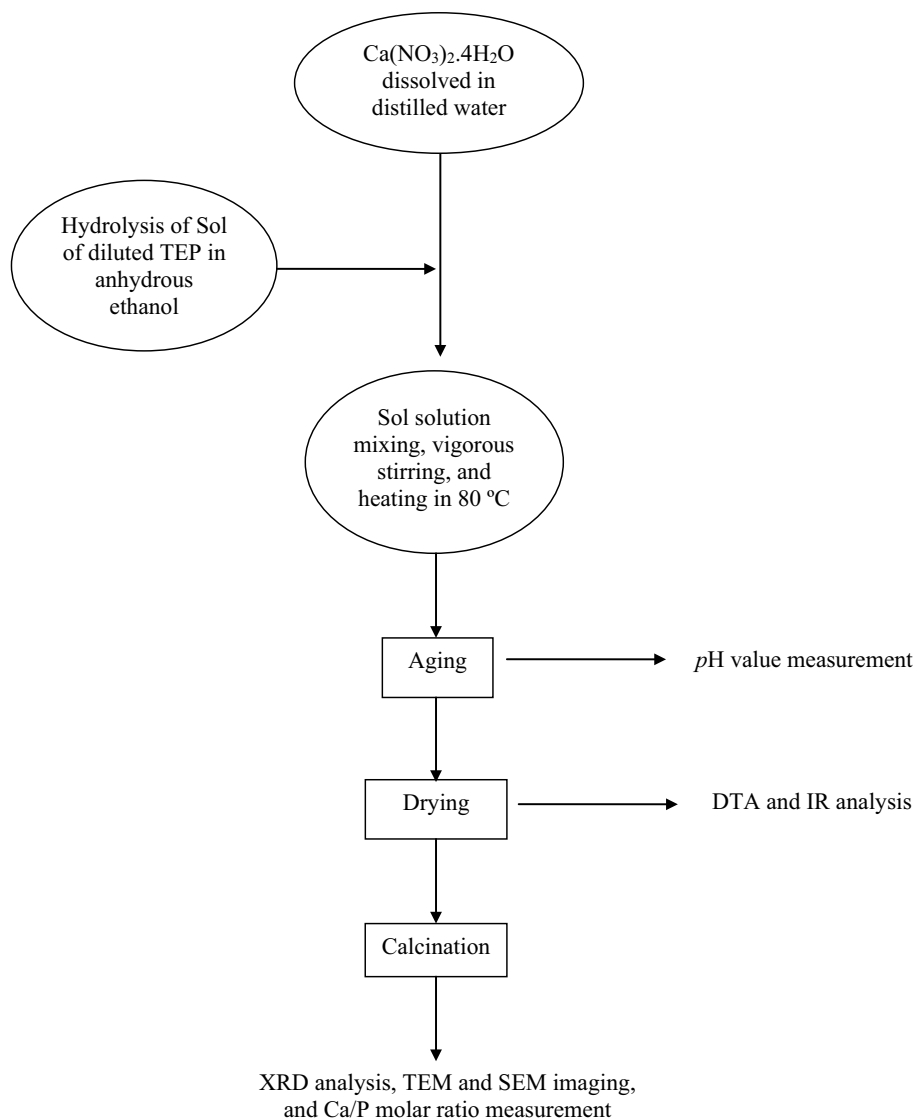


Fig. 1 X-ray diffraction patterns of samples **a S1**; **b S2–S5** calcined at 300, 400, 500, 600, and 700 °C, respectively, shown: (filled square) HA; (open square) CaO; (filled triangle) β-TCP; (open diamond) Ca₂P₂O₇; (filled circle) Ca(NO₃)₂; and (open circle) Ca(NO₃)₂·2(H₂O)

solution during 24 h aging show a decreasing pH from ~5.4 to 4.1. Moreover, increasing the temperature of the solution and aging time generally help to more complete the polymerization process [21].



However, incomplete polymerization between Ca and P precursors (Eq. 2) caused the formation of calcium oxide (CaO) and calcium carbonate (CaCO₃) impurities. Moreover, herein, the influence of firing temperature on phase purity and particle size of the synthesized HA has been studied. XRD patterns show intense peaks of CaO and HA (Fig. 1). The applied sol–gel approach for all samples are similar; therefore, their Ca/P molar ratio and CaO-to-HA ratio are same which could be obtained from peak height

Scheme 1 Flow sheet of HA sol–gel preparation approach**Table 1** Compositions and processing variables of precursors and comparison of XRD peak height ratios, CaO (200) versus HA (211) for appropriate calcined samples

Sample	Temp. (°C)	Aging at R.T. (h)	Heat treatment temp. (°C)	Peak height ratio CaO(200)/HA(211)	Determined Ca/P molar ratio
S1	80	24	300	–	1.98
S2	80	24	400	0.278	1.98
S3	80	24	500	0.275	1.99
S4	80	24	600	0.270	2.00
S5	80	24	700	0.262	1.98

All peak heights are measured directly from XRD pattern using a metric ruler, considering the background subtraction. Ca/P molar ratio obtained from SEM

ratio CaO (200)/HA (211) (see Table 1; Fig. 1). These harmful impurity phases could be reduced through control of the aging and heat treatment steps of sol–gel technique. The detailed discussion could be seen in the literature [21, 41].

The IR spectrum is indicative of the presence of amorphous HA and calcium nitrate in as-prepared gel. The presence of intense bands attributed to stretching modes of the OEt group located at 1232 and 1370 cm^{-1} in the as-dried

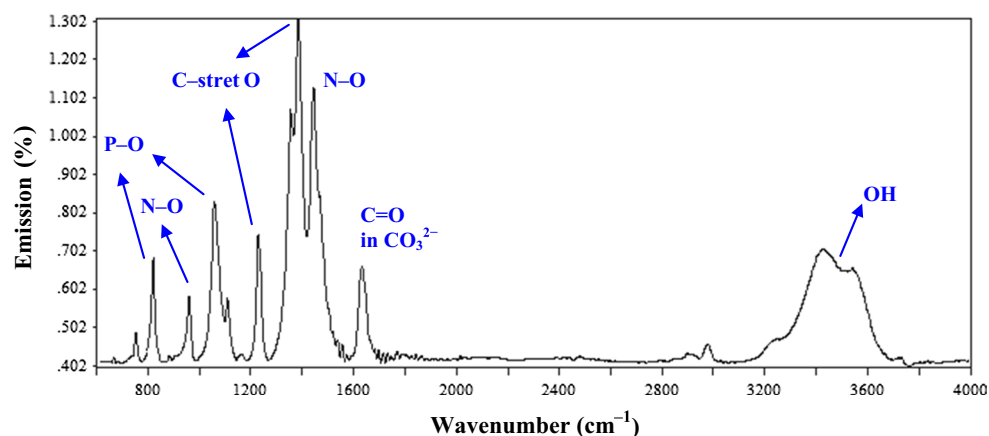
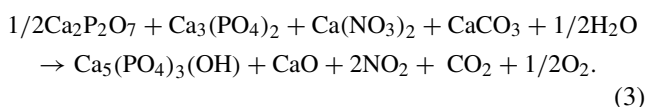


Fig. 2 IR spectrum of as-dried gel of sample **S5**. Wavenumber range of 500–4000 cm^{-1}

gel showed that the hydrolysis of TEP is incomplete. The bands located at 812, 1041, and 2995 cm^{-1} are ascribed to PO_4^{3-} bending and antisymmetric stretching vibrations, respectively [42], while the hydroxyl bending band at 3570 cm^{-1} supports the presence of HA in the as-dried gel (Fig. 2) [16]. The pale-yellow chunks of sample **S1** calcined at 300 °C was very hygroscopic because of the existence of unreacted calcium nitrate precursor in the gel as indicated by characteristic peaks in their XRD patterns and bands at 746, 910, and 1445 cm^{-1} which are assigned to NO_3^- in the as-dried gel (see Figs. 1a, 2). However, the band at 1680 cm^{-1} could be ascribed to carbonate.

In the DTA curve of the dried gel (Fig. 3), a weak exothermic peak at ~400 °C and a strong endothermic peak at 600 °C are seen [21, 22]. However, an intense exothermic peak at 310 °C is seen that is related to exiting gases containing nitrogen. The exothermic peak at ~400 °C is attributed to the crystallization of apatite phase. As another evidence for this claim, one can refer to XRD patterns (see Fig. 1b for **S2**) which confirm it as lowest crystallization temperature of HA. The driving force of apatite formation at 400 °C is lower than completion of the crystallization process, which caused intense XRD peaks of impurities to appear (see Fig. 1 for **S1** and **S2**). The endothermic DTA peak at 600 °C is related to the suggested reaction as below (Eq. 3):



On the other hand HA can crystallize either from amorphous apatite at ~400 °C or phase transformation and sometimes through combination of both paths where the firing temperature reaches about 600 °C or more (see Eq. 3) [40]. As it could be followed from XRD patterns (Fig. 1), the Ca–P impurity phases of **S4** and **S5** are reduced in comparison to **S2** and **S3** ones. It is notable that increasing the

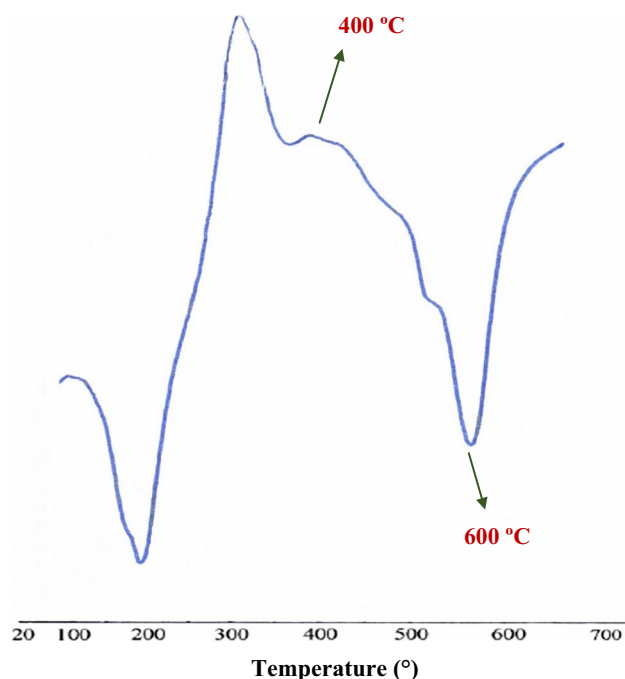
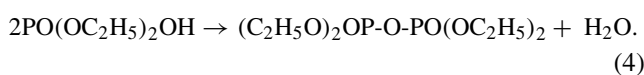


Fig. 3 DTA curve of the as-dried gel of samples

calcination temperature up to 700 °C results in the disappearance of pyrophosphate ($\text{Ca}_2\text{P}_2\text{O}_7$) and tricalcium phosphate (TCP) (Fig. 1). As is obvious from Eq. (2), the acidity of the mixed solution plays an essential role in the formation of more acidic Ca–Ps like TCP having lower Ca/P molar ratios than HA stoichiometry. The impurity $\text{Ca}_2\text{P}_2\text{O}_7$ may be formed from condensation between the particles of the phosphorus sol following formation of pyrophosphate (see Eq. 4) and XRD patterns verified its production (see Fig. 1b for **S2** and **S3**) [21].



Nanostructural examination

Amorphous materials because of high co-surface energy of their particles could start to crystallize through the calcination process. The particles size of gels prepared by low temperature sol–gel method is small with high surface energy that results in performing of crystallization along with drastic agglomeration and porosity. However, SEM images (not suitable for particle size determination) indicate remarkable

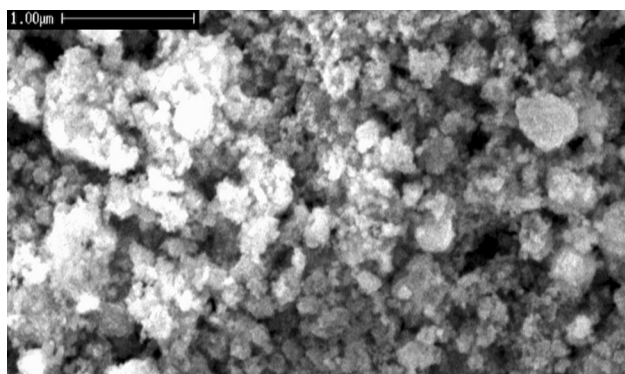


Fig. 4 Scanning electron micrograph of sample **S5** calcined at 700 °C shows highly agglomeration. Because of resemblance, images of other samples have been omitted

particle agglomeration which is unavoidable from sol–gel approach (Fig. 4, Just image of **S5** is depicted). Herein, two instruments TEM and XRD are used for particle size determination. TEM is certainly the most direct method, providing real images and impression of homogeneity of the particles. Although, the elaboration of size distribution curves is limited to the consideration of typically several hundreds of particles. Figure 5a–d shows typical TEM images of **S2–S5** HA powder samples. As it can be seen, raising the firing temperature from 400 up to 700 °C led to particles size growth. Nevertheless an important advantage of X-ray diffraction is providing a very simple possibility for estimating the particle size from the broadening of the XRD reflections by means of the so-called Scherrer formula (see Eq. 5) [23, 34]:

$$D = K\lambda / [W\cos(\theta)] \quad (5)$$

where K is constant which depends on the particle morphology and varies from 0.89 to 1.39 rad. Here it used consistently at 0.9, which corresponds to an average volume of the apparent size, D , independent of a peculiar morphology [43]. The λ is the Cu $K\alpha$ radiation (0.1544 nm), W is the full width at half-maximum, and θ is the diffraction angle (°). However, this technique requires several corrections and deconvolutions to reach reliable particle size

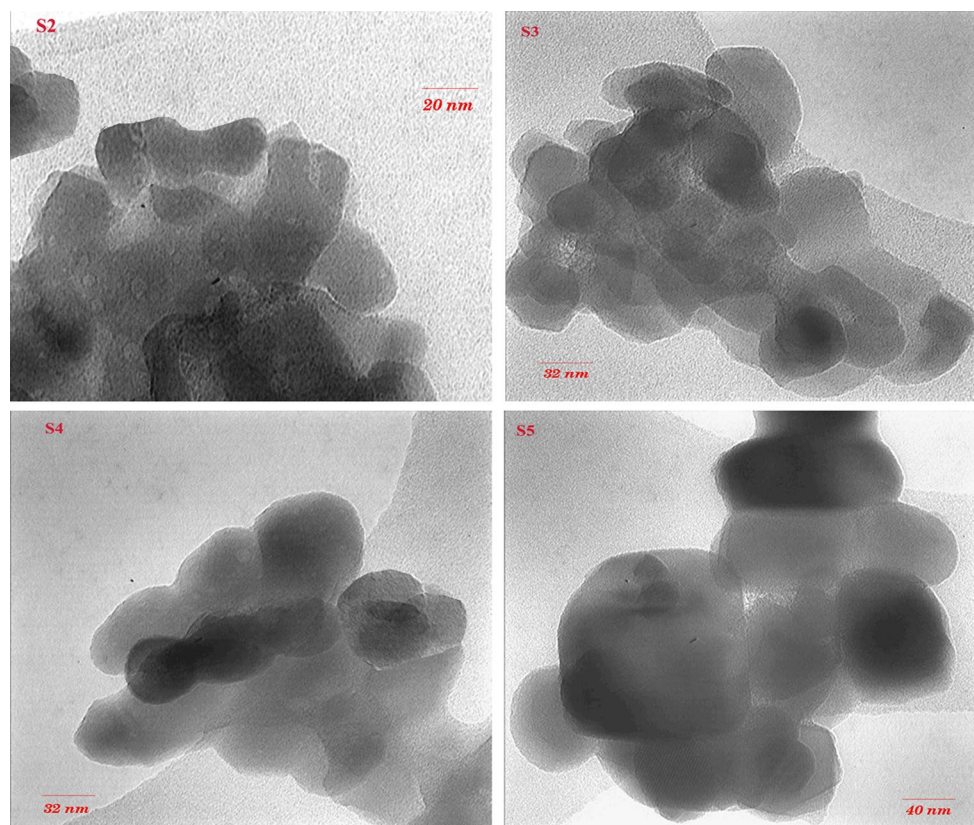


Fig. 5 TEM images of samples **S2–S5** calcined at 400, 500, 600, and 700 °C, respectively

Table 2 Comparison of XRD results using Gauss correction for instrumental broadening

Sample	Firing temp. (°C)	Williamson–Hall		Scherrer	
		<i>D</i> /nm	Micro-strain (°)	<i>D</i> (002)/nm	<i>D</i> (211)/nm
S1	300	–	–	–	–
S2	400	24.8	3.25E–3	35.4	21.1
S3	500	39.5	2.90E–3	30.5	27.3
S4	600	49.6	2.61E–3	34.1	36.8
S5	700	93.4	2.24E–3	65.7	50.4

values, i.e., $K\alpha$ radiation and instrumental line broadening have to be taken into account. It can be pointed out, based on the Scherrer formula (Eq. 5) and Fig. 1, that increasing the firing temperature is increasing the sharpness of XRD peaks indicating an increase in the particle size. Because the peaks monotonically and asymmetrically broaden, the particle size distribution shifts to larger average values through raising of firing temperature. According to TEM images (see Fig. 5), domain particle size of samples heated at 400, 500, 600, and 700 °C range from 18 to 30 nm, 35 to 50 nm, 40 to 65 nm, and 70 to 120 nm, where their mean size are 25, 40, 50, and 90 nm, respectively. These results are in good agreement with the calculated results from XRD patterns as is discussed below (Table 2). The reflection broadening in the XRD pattern is attributed to the contributions of crystallite size, micro-strain, and the instrument itself [43]. For a detailed analysis and comparison of peak broadening and data processing, see the review by Balzar [44]. Instrumental broadening arising from slit width, penetration in sample, imperfect monochromaticity, and imperfect focusing is generally observed. This broadening is equal for all samples which are analyzed with the same instrument. To correct for instrumental broadening, a standard microcrystalline quartz sample with a large enough particle size (10 μm) is used to eliminate particle size and micro-strain broadening. Its peak width value (W) of $\sim 0.12^\circ$ (0.0026 radians) is obtained which just relates to instrumental broadening. To deconvoluted size and instrumental effects, two simplified methods are generally applied, the Cauchy (Eq. 6) or Gauss approximation (Eq. 7) [35, 43].

$$W = W_{\text{sample}} - W_{\text{standard reference}} \quad (6)$$

$$W = \left(W_{\text{sample}}^2 - W_{\text{standard reference}}^2 \right)^{0.5} \quad (7)$$

The additional line broadening due to micro-strain ϵ_s can be expressed according to Stokes and Wilson [45].

$$W_\epsilon = 4\epsilon_s \tan \theta \quad (8)$$

Combination of Eqs. (5) and (8) with attention to Eq. (6) or (7), results in Eqs. (9) or (10), respectively.

$$W \cos \theta = K\lambda/D + 4\epsilon_s \sin \theta \quad (9)$$

$$(W \cos \theta)^2 = (K\lambda/D)^2 + 16\epsilon_s^2 \sin^2 \theta \quad (10)$$

Separation of the two broadening effects is possible by the so-called W–H plot of $W \cos \theta$ versus $\sin \theta$ or $(W \cos \theta)^2$ versus $\sin^2 \theta$ [44]. Herein, an excellent correlation is obtained with the Gauss approximation (Eq. 10). Therefore, Eq. (10) was applied to the (002), (210), (211), (300), and (310) reflections. Correlated W–H plots are shown in Fig. 6. The results are summarized in Table 2. Raising of the firing temperature results in crystallite size (D) increasing and micro-strain decreasing. Permanent increasing of D at 700 °C indicates this temperature as a suitable sintering temperature for the HA phase. In most references, only one reflection was used to calculate crystallite size with the Scherrer equation [33, 45] without considering the contribution of micro-strain to the widening of reflections and no reasonable explanation for big difference of crystallite size calculated from different reflections with Scherrer equation. The calculated particle size of S2–S5 by not modified Scherrer's formula within (002) and (211) reflections is not in the same value range (see Table 2).

Summary and conclusion

In this work, small nanoparticle of HA powders through a low temperature sol–gel method including new conditions were synthesized and their structural evolution and particle size evaluation investigated. Phase evolution from sol-to-gel and from gel-to-ceramic was studied using XRD, IR, and DTA analyses. Impurity phases such as CaO, CaCO_3 , and Ca–P form if the aging and especially firing temperature not properly controlled. The CaO phase was formed from the decomposition of undesirable $\text{Ca}(\text{NO}_3)_2$ precipitate during the calcinations process. During the aging step, Ca^{2+} and NO_3^- ions react with hydrolyzed TEP resulting in formation of a complex that is stabilized in the subsequent drying step. DTA and XRD patterns of the synthesized HA powders indicated the crystallization of HA has begun at the low temperature of 400 °C. This is because of more completed reaction between Ca and hydrolyzed P precursors through the novel sol–gel technique. High surface energy of small gel particles is an alternative reason for such low crystallization temperature. XRD and TEM methods were applied for particle size determination of sol–gel-derived nanocrystallite HA in the low mean size of 25–100 nm. All techniques within particle size evaluation have their respective advantages, but can also produce specific artifacts. The advantage of TEM is the direct observation. Since sol–gel approach results in particles agglomeration, small particles may be overlooked or can

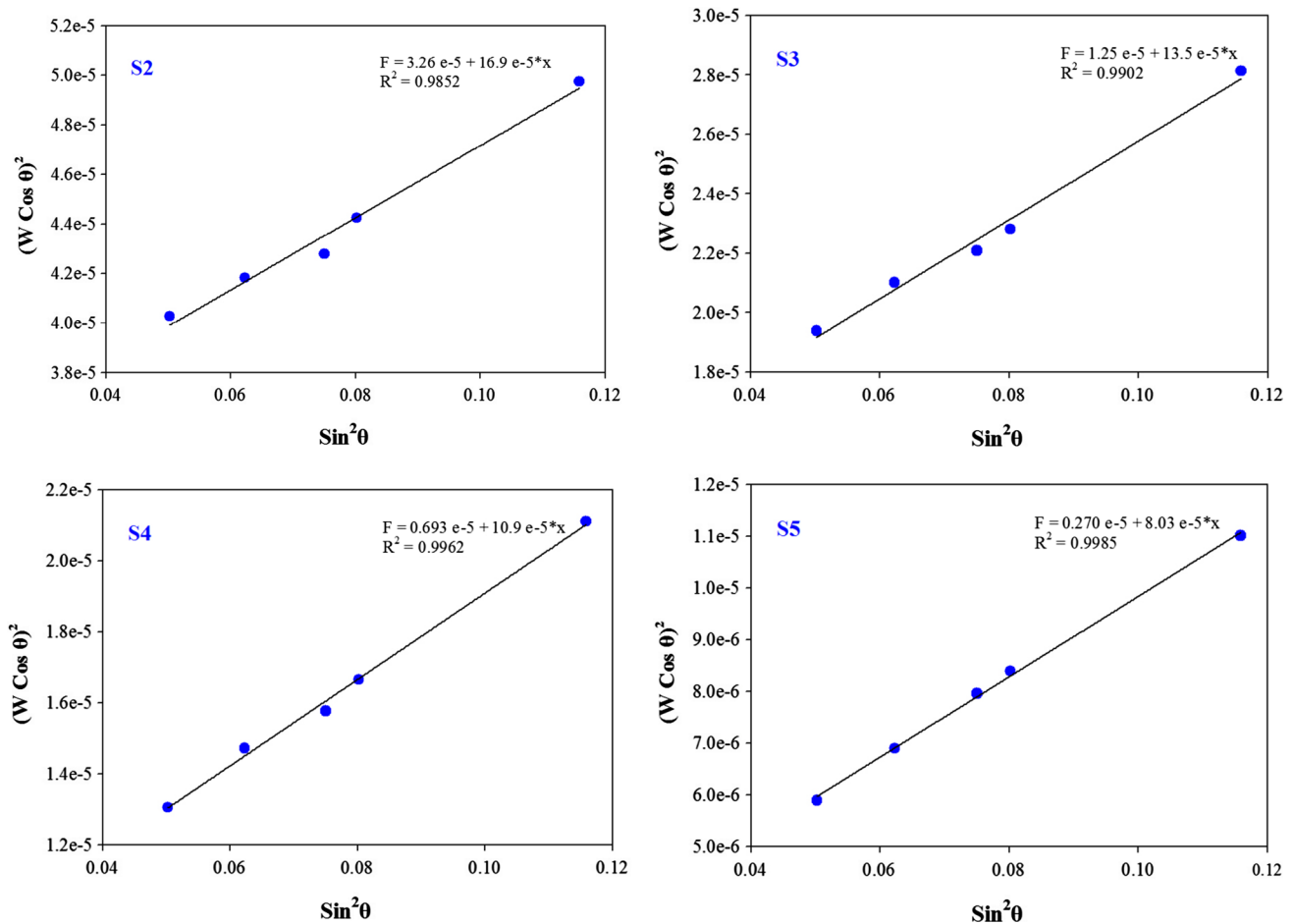


Fig. 6 Deconvolution of strain and size effects of S2–S5 using Gauss approximation, by Williamson–Hall equation

be difficult to distinguish in agglomerates. Scherrer's equation and W–H plot was used in order to separate the effect of crystallite size and micro-strain on reflection broadening which gave a crystallite size in relatively good agreement with TEM. But, the results obtained with Scherrer's formula on a peak are artifact. The mean crystallite size increased and micro-strain decreased significantly with raising of the firing temperature from 400 to 700 °C. Almost a fourfold increase in the mean crystallite size, D at 700 °C in comparison with 400 °C from about 25 to 100 nm, suggests this temperature as suitable sintering temperature.

Acknowledgements MCH wishes to thank to the Hakim Sabzevari University (HSU) for financial support of this article.

References

1. A.S. Posner, *Physiol. Rev.* **49**(4), 760–792 (1969)
2. M.J. Glimcher, *Philos. Trans. R. Soc. Lond.* **304B**, 479–508 (1984)
3. M. Vallet-Regi, J.M. Gonzalez-Calbet, *Prog. Solid State Chem.* **32**, 1–31 (2004)
4. E.E. Berry, *J. Inorg. Nucl. Chem.* **29**, 317–327 (1967)
5. J.E. Easton, The chemical composition of bone, in *Biochemists Handbook*, ed. by C. Long (Princeton, Van Nostrand, 1961), pp. 715–720
6. A. Carradò, N. Viart, *Solid State Sci.* **12**, 1047–1050 (2010)
7. X. Guo, H. Yan, S. Zhao, Z. Li, Y. Li, X. Liang (2013) *Adv. Powder Technol.* doi:10.1016/j.apt.2013.03.002
8. J. Klinkaewnarong, E. Swatsitang, S. Maensiri, *Solid State Sci.* **11**, 1023–1027 (2009)
9. R.H.R. Castro, K. van Benthem (eds.), *Sintering: Mechanisms of Conventional Nanodensification and Field Assisted Processes* (Springer, Berlin, 2013), pp. 1–16
10. H. Eshtiagh-Hosseini, M.R. Housaindokht, M. Chahkandi, A. Youssefi, *J. Non-Cryst. Sol.* **354**, 3854–3857 (2008)
11. D.-H. Baek, J.-K. Kim, Y.-J. Shin, G.S. Chauhan, J.-H. Ahn, K.-W. Kim, *J. Power Sources* **189**, 59–65 (2009)
12. U. Chaimongkon, A. Thongtha, T. Bongkarn, *Curr. Appl. Phys.* **11**, S70–S76 (2011)
13. N. Das, H.S. Maiti, *J. Membr. Sci.* **140**, 205–212 (1998)
14. C.J. Tredwin, G. Georgiou, H.-W. Kim, J.C. Knowles, *Dent. Mater.* **29**, 521–529 (2013)
15. M. Kamitakahara, R. Imai, K. Ioku, *Materials Science and Engineering*. C 33 (2013) 2446–2450

16. W. Weng, J.L. Baptista, J. Eur. Ceram. Soc. **17**, 1151–1156 (1997)
17. K. Cheng, W. Weng, G. Han, P. Du, G. Shen, J. Yang, J.M.F. Ferreira, Mater. Chem. Phys. **78**, 767–771 (2003)
18. K. Cheng, W. Weng, G. Han, P. Du, G. Shen, J. Yang, J.M.F. Ferreira, Mater. Res. Bull. **38**, 89–97 (2003)
19. E.K. Girija, G.S. Kumar, A. Thamizhavel, Y. Yokogawa, S.N. Kalkura, Powder Technol. **225**, 190–195 (2012)
20. M. Aminzare, A. Eskandari, M.H. Baroonian, A. Berenov, Z. Razavi Hesabi, M. Taheri, S.K. Sadrnezhad, Ceram. Int. **39**, 2197–2206 (2013)
21. H. Eshtiagh-Hosseini, M.R. Housaindokht, M. Chahkandi, Mater. Chem. Phys. **106**, 310–316 (2007)
22. D.M. Liu, T. Troczynski, W.J. Tseng, Biomaterials **22**, 1721–1730 (2001)
23. W. Weng, G. Shen, G. Han, J. Mater. Sci. Lett. **19**, 2187–2188 (2000)
24. A. Montener, G. Gnappi, F. Ferrari, M. Cesari, M. Fini, J. Mater. Sci. **35**, 2791–2797 (2000)
25. B. Mavis, A.C. Tas, J. Am. Ceram. Soc. **83**, 989–991 (2000)
26. F. Scalera, F. Gervaso, K.P. Sanosh, A. Sannino, A. Licciulli, Ceram. Int. **39**, 4839–4846 (2013)
27. F. Bakan, O. Laçin, H. Sarac, Powder Technol. **233**, 295–302 (2013)
28. C.F. Feng, K.A. Kohr, E.J. Liu, P. Cheang, Scr. Mater. **42**, 103–109 (2000)
29. A.K. Lynna, D.L. DuQuesnay, Biomaterials **23**, 1947–1953 (2002)
30. T. Goto, I.Y. Kim, K. Kikuta, C. Ohtsuki, Ceram. Int. **38**, 1003–1010 (2012)
31. D.-H. Kim, H.-H. Chun, J.D. Lee, S.-Y. Yoon, Ceram. Int. **40**, 5145–5155 (2014)
32. H. Borchert, E.V. Shevchenko, A. Robert, I. Mekis, A. Kornowski, G. Grübel, H. Weller, Langmuir **21**, 1931–1936 (2005)
33. G.K. Williamson, W.H. Hall, Acta Metall. **1**, 22–31 (1953)
34. P. Scherrer, Nachr. Ges. Wiss. Göttingen, *Math.-Phys. Kl* **2** (1918) 98–100
35. A. Weibel, R. Bouchet, F. Boulc’h, P. Knauth, Chem. Mater. **17**, 2378–2385 (2005)
36. A. Deptula, W. Lada, T. Olczak, A. Borello, C. Alvani, A. di Bartolomeo, J. Non-Cryst. Solids **147**(148), 537–541 (1992)
37. L.D. Piveteau, M.I. Girona, L. Schlapbach, P. Barboux, J.P. Boilot, B. Gasser, J. Mater. Sci. Mater. Med. **10**, 161–167 (1999)
38. K.A. Gross, C.S. Chai, G.S.K. Kannangara, B. Bin-Nissan, L. Hanley, J. Mater. Sci. Mater. Med. **9**, 839–843 (1998)
39. A. Jilavenkatesa, R. A. Condrate Sr., J. Mater. Sci. **33**, 4111–4119 (1998)
40. D.M. Liu, T. Troczynski, W.J. Tseng, Biomaterials **23**, 1227–1236 (2002)
41. C.M. Lopatin, V. Pizziconi, T.L. Alford, T. Laursen, Thin Solid Films **326**, 227–232 (1998)
42. L.-Y. Huang, K.-W. Xu, J. Lu, J. Mater. Sci. Mater. Med. **11**, 667–673 (2000)
43. H.P. Klug, L.E. Alexander, *X-Ray Diffraction Procedure for Polycrystalline and Amorphous Materials* (Wiley, New York, 1974)
44. D. Balzar, *Defect and Microstructure Analysis from Diffraction* (Oxford University Press, New York, 1999)
45. E. Tkalcec, M. Sauer, R. Nonninger, H. Schmidt, J. Mater. Sci. **36**, 5253–5263 (2001)